Journal of ELECTRONIC MATERIALS, Vol. 35, No. 1, 2006 *Special Issue Paper*

Phase Field Simulations of Morphological Evolution and Growth Kinetics of Solder Reaction Products

K.K. HONG[1] and J.Y. HUH[1,2]

1.—Department of Materials Science and Engineering, Korea University, Seoul 136-713, Korea.
2.—E-mail: jyhuh@korea.ac.kr

Two-dimensional simulations of the morphological and growth evolutions of the intermetallic compound (IMC) formed between a Sn-based solder and a Cu pad are performed using a multiphase field model, in order to examine the difference between the IMC growth behavior for the soldering reaction and that for the solid-state aging after soldering. The simulations show that the scallop-type IMC morphology formed in the soldering reaction is governed not only by the surface energy difference between the solder/IMC interface and the IMC grain boundary (GB), but also by the difference in diffusivities in the liquid solder and the IMC GB. It is also shown that the orders of magnitude difference in the IMC growth rate between the soldering reaction and the subsequent aging process is mainly attributed to the increased IMC GB distance resulting from the morphological change of the IMC from a scallop type to a layer type. The change in the solder diffusivity itself, however, has only a minor influence on the IMC growth kinetics of the layer-type IMC in the subsequent aging process.

Key words: Phase field simulation, solder reaction, intermetallic compound (IMC), morphology, growth kinetics, grain boundary (GB) diffusion

INTRODUCTION

The interfacial reaction between solder and metallization is an essential process in modern microelectronic packaging technology for interconnections. During soldering or reflow processes using a Sn-based solder, an intermetallic compound (IMC) layer is formed between the molten solder and the solid metallization pad. The IMC continues to grow during subsequent solid-state aging in device use at temperatures below the melting point of the solder. Since the morphology and thickness of the IMC layer strongly affect the mechanical properties of the solder joints,[1–4] reliability tests of the solder joints require solid-state aging to be performed, typically at 150°C for 1,000 h. With the trend in packaging moving toward the ball-grid-array (BGA) type package, employing solder balls with a reduced size and thin-film metallization, the yield and reliability issues of the solder joints have drawn extensive studies on the morphology and kinetics of IMC formation in the soldering and solid-state aging processes.[5–8]

(Received April 19, 2005; accepted August 1, 2005)

It has been known that there are large differences between the morphology and kinetics of IMC formation for the soldering reaction and those for solid-state aging after soldering. In soldering reactions between most Sn-based solders and Cu metallizations, the Cu_6Sn_5 (η) IMC is formed as scallop-type grains with liquid solder penetrating between them.[9–11] This scallop-type IMC grows rapidly with growth rates on the order of several microns per minute during the solder reaction. At the same time, the IMC grains coarsen and decrease in number with increasing soldering reaction time, which results in the growth kinetics of the scallop-type IMC having a $t^{1/3}$ dependence on time.[9,12,13] During the subsequent solid-state aging process, the scallop-type IMC morphology changes to a layer type and the growth rate of the layer-type IMC becomes several orders of magnitude lower than that for the soldering reactions.[10] Together with the morphological change, the time dependence of the IMC growth kinetics is also known to change from $t^{1/3}$ to $t^{1/2}$ for the solid-state aging process.[10,14,15]

There are two issues of basic interest related to the formation of the IMCs during the soldering re-

action and the solid-state aging process. One is the question of what governs the difference in the IMC morphology between these two kinds of solder reaction and the other is how the morphological change affects the IMC growth kinetics. Tu et al. examined the stability criteria for the scallop-type IMC morphology in the soldering reaction and the layer-type IMC morphology in the solid-state aging process, based on the energetics minimizing the solder/IMC interface and IMC grain boundary (GB) energies.[11] However, the IMC morphology formed during the growth evolution can also be dictated by kinetic factors, such as the dominant diffusion mechanisms for IMC growth, but this has not been taken into account in previous studies. It is not yet clearly understood either how the morphological change is related to the orders of magnitude difference in the growth kinetics between the soldering and solid-state aging processes.

In the present work, phase field simulations were performed for the morphological and growth evolution of the Cu_6Sn_5 IMC formed between a Sn-based solder and Cu pad during the soldering and solid-state aging processes. The simulations showed that the formation of the scallop-type IMC morphology in the soldering reaction is governed not only by the ratio of the solder/IMC interface energy to the IMC GB energy, but also by the ratio of the IMC GB diffusivity to the liquid solder diffusivity. It is also shown that the orders of magnitude difference in the IMC growth rate between the soldering and aging processes is correlated with the difference in the diffusional flux along the IMC GB caused by the morphological difference between these two processes. The difference in the solder diffusivity between the two processes is found to have only a minor effect on the IMC growth kinetics.

PHASE FIELD SIMULATION

We consider the microstructural evolution of the multigrained Cu_6Sn_5 IMC layer formed between a Sn-Cu solder and Cu pad during the soldering reaction at 250°C and during the subsequent solid-state aging process at 180°C. For simplicity, the formation of Cu_3Sn between the Cu_6Sn_5 IMC and Cu pad is ignored. Therefore, the evolving system considered here is an isothermal Sn-Cu binary system with three phases, consisting of the Sn-rich solder, multigrained Cu_6Sn_5 (η), and Cu (α). The solder can be either in the liquid state (L) during the soldering reaction or in the solid state (S) during the solid-state aging process. Since the use of the phase field simulation technique to describe such a system has been reported previously, only a brief description is given in this section. For more details, the reader is referred to Reference 16.

Formulation

The spatial distribution of the Cu (α) pad, N different η-IMC grains, and solder phase (L or S) in the system at a given time (t) are described by the phase field variables, $\phi_0(\vec{x},t)$, $\phi_j(\vec{x},t)$ (; j = 1, . . . , N), and $\phi_{N+1}(\vec{x},t)$, respectively. The phase field variable ϕ_i can be considered as the local fraction of the phase (or grain) designated by the subscript, and, thus, the N + 2 phase field variables at any position in the system are subjected to the constraint of $\sum_{i=0}^{N+1}\phi_i(\vec{x},t) = 1$. In this way, the interfaces and grain boundaries are represented by the regions in which more than one phase field variable varies in the range between zero and one. The phase compositions $c_i(\vec{x},t)$, in terms of the mole fraction of Sn, of the coexisting phases at a given position in the interface regions are related to the local composition $c(\vec{x},t)$ by the local mass conservation condition: $\sum_{i=0}^{N+1}\phi_i(\vec{x},t)c_i(\vec{x},t) = c(\vec{x},t)$.

The total free energy functional of the system can then be expressed as[17,18]

$$F[c(\vec{x},t),\phi_k(\vec{x},t)] = \int_V \left[\sum_{i=0}^{N+1}\sum_{j=i+1}^{N+1} \left\{ \phi_i f_i(c_i) - \frac{\varepsilon_{ij}^2}{2}\nabla\phi_i \cdot \nabla\phi_j + \omega_{ij}\phi_i\phi_j \right\} - \lambda_\phi \left(\sum_{i=0}^{N+1}\phi_i - 1 \right) \right] dV \tag{1}$$

where f_i is the chemical free energy density of phase i, and λ_ϕ is the Lagrange multiplier for the constraint among the N + 2 phase field variables. The terms ε_{ij} and ω_{ij} are the positive parameters that are related to the energy σ_{ij} and width w_{ij} of the interface (or GB) between the ϕ_i = 1 and ϕ_j = 1 phases (or grains) by

$$\varepsilon_{ij} = \frac{\sqrt{8\sigma_{ij}w_{ij}}}{\pi} \quad \text{and} \quad \omega_{ij} = \frac{4\sigma_{ij}}{w_{ij}} \tag{2}$$

At a position specified with a set of c and ϕ_i (; i = 0, . . . , N + 1), the phase compositions $c_i(\vec{x},t)$ of the coexisting phases can be found from the additional condition that all of the coexisting phases have an identical diffusion potential:

$$\frac{df_0}{dc_0} = \frac{df_1}{dc_1} = \ldots = \frac{df_{N+1}}{dc_{N+1}} \equiv f_c(c,\phi_i) \tag{3}$$

The evolution equations of the composition field $c(\vec{x},t)$ and the phase fields $\phi_i(\vec{x},t)$, which guarantee a monotonic decrease of the free energy functional F, take the following forms:[17,18]

$$\frac{\partial c}{\partial t} = \nabla \cdot \left[D(\phi_i)\sum_{i=0}^{N+1}\phi_i\nabla c_i \right] \tag{4}$$

and

$$\frac{\partial\phi_i}{\partial t} = -\frac{2}{p}s_i\sum_{j\neq i}^{N+1}s_jM_{ij}\left(\frac{\delta F}{\delta\phi_i} - \frac{\delta F}{\delta\phi_j}\right) \tag{5}$$

with

$$\frac{\delta F}{\delta\phi_k} = \sum_{l\neq k}^{N+1}\left\{\frac{\varepsilon_{kl}^2}{2}\nabla^2\phi_l + \omega_{kl}\phi_l\right\} + \{f_k(c_k) - c_kf_c\} - \lambda_\phi \tag{6}$$

where D in Eq. 4 is the interdiffusion coefficient that depends on the set of ϕ_i. In Eq. 5, s_i is a step function

defined as $s_i(\vec{x},t) = 1$ if $\phi_i(\vec{x},t) > 0$ and $s_i(\vec{x},t) = 0$ if $\phi_i(\vec{x},t) = 0$, p is also a step function defined as $p(\vec{x},t) = \Sigma_{i=0}^{N+1} s_i(\vec{x},t)$, and M_{ij} is the mobility of the interface (or GB) between the $\phi_i = 1$ and $\phi_j = 1$ phases (or grains). The notation $\Sigma_{j\neq i}^{N+1}$ is used to imply the summation from $j = 0$ to $j = N + 1$, except for $j = i$.

Numerical Procedure

Before performing the simulations, assuming that all of the interfaces and the GB have the same width, $w_{ij} = w$, the evolution Eqs. 4 and 5 were first nondimensionalized using a scaled position vector, $\vec{z} \equiv \vec{x}/w$, and time, $\tau \equiv D_L t/w^2$, where D_L is the interdiffusion coefficient of the solder in the liquid state. Accordingly, $D(\phi_i)$ and M_{ij} in Eqs. 4 and 5 were replaced by the relative diffusivity, $\overline{D}(\phi_i) \equiv D(\phi_i)/D_L$, and interface (or GB) mobility, $\overline{M}_{ij} \equiv M_{ij}/D_L$, respectively. The simulations are then performed by solving the nondimensionalized Eqs. 4 and 5 numerically, using an explicit, finite-difference scheme. The material parameters given in Table I are employed for the simulations of the soldering reaction and the solid-state aging process, unless otherwise indicated.

For the chemical free energy densities of the individual phases (f_L, f_S, f_η, and f_α), we used the data obtained from the CALPHAD method.[19] However, since the η-IMC was described as a stoichiometric compound in the literature, we assumed f_η to be a parabolic function of composition, so that the η-IMC phase could have a range of solubility. The equilibrium phase compositions calculated from the free energy densities at 250°C and 180°C are given in Table II, in which $c_\eta^{\eta S}$, for example, denotes the composition of the η-IMC in equilibrium with the solid-state solder (S).

For the explicit, finite-difference scheme, the nondimensionalized forms of Eqs. 4 and 5 were discretized using Euler formulas for the time derivatives and five point, central difference formulas for the spatial derivatives. The dimensionless grid spacing was $\Delta z_1 = \Delta z_2 = 0.25$ (≡h), and the dimensionless time-step was $\Delta\tau = 1.25 \times 10^{-2}$ for the soldering reaction and $\Delta\tau = 1.25 \times 10^{2}$ for the solid-state aging process. The simulations were carried out using two different computational cells: $z_1 \times z_2 = 16h \times 90h$ with $N = 2$ and $z_1 \times z_2 = 184h \times 90h$ with $N = 30$. The former computational cell with two IMC grains ($N = 2$) was used to test the morphological evolution caused by the penetration of liquid solder along the η-IMC GB in the soldering reaction. The latter computational cell with 30 IMC grains ($N = 30$) was used to examine the growth evolution of the η-IMC in the soldering and aging reactions.

Table I. Typical Material Parameters Employed in the Present Study

Parameters	Soldering (250°C)	Aging (180°C)
$\overline{D}_L$ or $\overline{D}_S$	1	1.0×10^{-4}
$\overline{D}_{L/\eta}$ or $\overline{D}_{S/\eta}$	1.0×10^{-1}	1.0×10^{-5}
$\overline{D}_{GB}$	1.0×10^{-4}	1.0×10^{-5}
$\overline{D}_{\eta/\alpha}$	1.0×10^{-3}	1.0×10^{-5}
$\overline{D}_\eta = \overline{D}_\alpha$	1.0×10^{-6}	1.0×10^{-6}
$\sigma_{L/\eta}$ or $\sigma_{S/\eta}$ (mJ/m^2)	100	250
σ_{GB} (mJ/m^2)	300	300
$\sigma_{\eta/\alpha}$ (mJ/m^2)	500	500
$\overline{M}_{L/\eta}$ or $\overline{M}_{S/\eta}$	1.0×10^{6}	7.0×10^{2}
$\overline{M}_{\eta/\alpha} = \overline{M}_{GB}$	7.0×10^{3}	7.0×10^{2}

Table II. Equilibrium Phase Compositions in Mole Fraction at the Soldering and Aging Temperatures

Equilibrium Phase Composition	Soldering (250°C)	Aging (180°C)
$c_L^{L\eta}$ or $c_S^{S\eta}$	0.977	0.991
$c_\eta^{\eta L}$ or $c_\eta^{\eta S}$	0.441	0.446
$c_\eta^{\eta\alpha}$	0.388	0.381
$c_\alpha^{\alpha\eta}$	0.195	0.171

At the beginning of the simulation, a continuous array of rectangular IMC grains was placed in $41h \leq z_2 \leq 45h$ between the solder at the top and the α-Cu at the bottom. The two IMC grains for the case of $N = 2$ had the same width. However, for the case of $N = 30$, the grain widths were randomly sized between 4h and 8h. As the initial conditions for the composition field, the compositions of the liquid solder, η-IMC, and α-Cu regions were taken to be uniform as $c_L^{L\eta}$, $(c_\eta^{\eta L} + c_\eta^{\eta\alpha})/2$, and 0.02, respectively. The boundary conditions for c and ϕ_i (; $i = 0, \ldots, N + 1$) along the z_1-axis were of the Neumann type for the case of $N = 2$, but periodic for the case of $N = 30$. The boundary conditions along the z_2 axis were the same for both cases, viz. Neumann type at the bottom ($z_2 = 0$) of the α-Cu and Dirichlet type at the top ($z_2 = 90h$) of the solder.[16] The simulations were performed until neither the solder nor the α-Cu was completely consumed by the growing η-IMC.

RESULTS AND DISCUSSION

Formation of Scallop-Type IMC Morphology in Soldering Reactions

The scallop-type morphology of the η-IMC formed in soldering reactions manifests itself in the form of deep liquid solder penetration in between the IMC grains. The scallop-type η-IMC morphology changes to the layer type during the subsequent solid-state aging process, when the solder channel in between the IMC grains is replaced by the IMC GB. Since the soldering and aging processes differ by the state of the solder (liquid or solid), the morphological change between the two processes should be attributed to those material parameters that depend on the state of the solder. Obviously, the solder diffusivity and solder/IMC interface energy are included among these material parameters. In this subsection, we discuss the simulations that were performed at 250°C using a computational cell with two, equal-

sized η-IMC grains, in order to examine how the liquid solder diffusivity (D_L) and the liquid solder/IMC interface energy ($\sigma_{L/\eta}$) influence the penetration behavior of the liquid solder in between the two IMC grains.

Effect of the diffusivity ratio (D_{GB}/D_L) between the IMC grain boundary and liquid solder

Since, in the current study, the diffusivities are scaled with respect to the liquid solder diffusivity, decreasing the liquid solder diffusivity by one order of magnitude, for example, is equivalent to increasing all of the relative diffusivities other than $\bar{D}_L = 1$ by one order of magnitude. Therefore, the dependence of the penetration behavior of the liquid solder between the IMC grains on the liquid solder diffusivity is examined first, by employing those relative diffusivities given in Table I (for the case where $\bar{D}_{GB} = 10^{-4}$) and then by employing all the relative diffusivities (except $\bar{D}_L = 1$) increased by one and two orders of magnitude from those in Table I (for the cases where $\bar{D}_{GB} = 10^{-3}$ and 10^{-2}, respectively). It is noted from Table I that, since $2\sigma_{L/\eta} < \sigma_{GB}$, the complete wetting of the IMC GB by the penetration of the liquid solder is energetically favorable.

Figure 1 shows the snapshots of the η-IMC morphology at the nondimensional times of $\tau = 5 \times 10^3$ and 2.5×10^4 and for the three cases: $\bar{D}_{GB} = 10^{-4}$, 10^{-3}, and 10^{-2}. Each snapshot was obtained by depicting the largest value of ϕ_i (; i = 1, . . . , N) at each nodal point in the grayscale. Thus, the gray region between the two η-IMC grains in the white contrast corresponds to the region of the IMC GB. When the liquid solder diffusivity (D_L) is much greater than the IMC GB diffusivity (D_{GB}), as in the case where $\bar{D}_{GB} = 10^{-4}$ shown in Fig. 1a, the liquid solder penetrates deeply between the two IMC grains and, thus, the IMC grains have scallop-type morphologies. However, when the liquid solder diffusivity is decreased, as in the cases where $\bar{D}_{GB} = 10^{-3}$ and 10^{-2}, the penetration of the liquid solder between the IMC grains becomes shallower and the IMC morphology becomes more like a layer-type morphology, even if $2\sigma_{L/\eta} < \sigma_{GB}$. With respect to the greater IMC growth in the case of a larger $\bar{D}_{GB}$ at a given nondimensional time (τ), it is noted that the nondimensional time corresponds to different real times (t) depending on the liquid solder diffusivity.

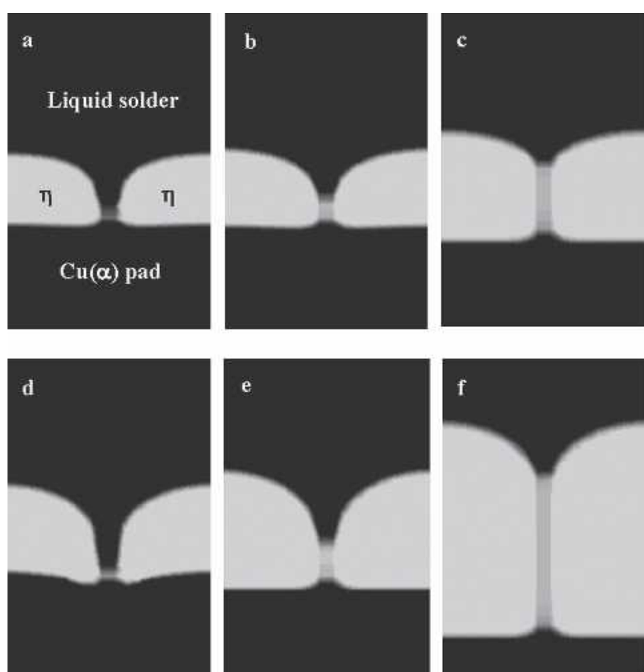

Fig. 1. Morphological evolutions of the η-IMC at 250°C for the three different cases of the diffusivity ratio between the liquid solder and the IMC GB: (a) and (d) $D_{GB}/D_L = 10^{-4}$, (b) and (e) $D_{GB}/D_L = 10^{-3}$, and (c) and (f) $D_{GB}/D_L = 10^{-2}$. Two snapshots for each of the three cases are shown as obtained at the nondimensional times: (a)–(c) $\tau = 5 \times 10^3$ and (d)–(f) $\tau = 2.5 \times 10^4$. For all three cases, $\sigma_{L/\eta}$ = 100 mJ/m^2 and σ_{GB} = 300 mJ/m^2 are assumed for the liquid solder/IMC interface energy and the IMC GB energy, respectively.

The ratio of the IMC thickness along the GB (Z_{GB}) to that at the center of a grain (Z_c) may be used as a measure of the IMC morphology, since a smaller value of Z_{GB}/Z_c indicates a deeper penetration of the liquid solder between the IMC grains and, thus, a more scallop-like IMC morphology. Figure 2 shows the changes in Z_{GB}/Z_c with (nondimensional) time τ for the three cases of $\bar{D}_{GB}$. The thickness ratio, which was initially $Z_{GB}/Z_c = 1$, quickly decreases in the early stages of the simulation to a value that is lower for the smaller $\bar{D}_{GB}$ case, and then changes only slightly afterward as the IMC grows.

Although all of the relative diffusivities were changed simultaneously by the same order of magnitude in the simulations corresponding to Figs. 1 and 2, nearly the same results were obtained by changing only the relative IMC GB diffusivity ($\bar{D}_{GB}$). Therefore, the penetration behavior of the liquid solder and, thus, the morphological changes of the η-IMC as a function of the liquid solder diffusivity, as shown in Figs. 1 and 2, are primarily dependent on the diffusivity ratio ($\bar{D}_{GB}$) between the IMC GB and the liquid solder.

The effect of the diffusivity ratio, D_{GB}/D_L, on the penetration of the liquid solder can be understood in

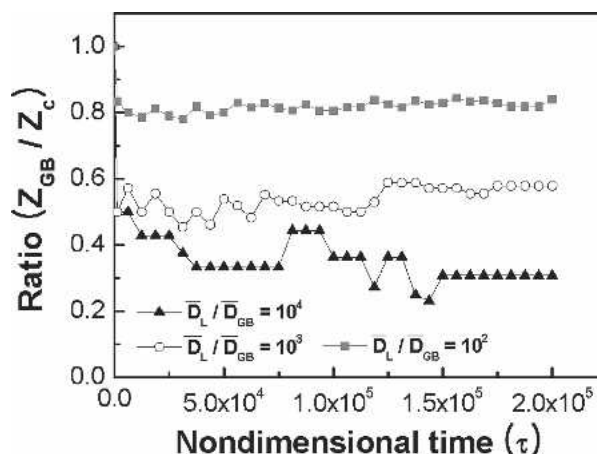

Fig. 2. Changes in the ratio of the IMC thickness along the GB (Z_{GB}) to that at the center of a grain (Z_c) with nondimensional time for the three cases: $D_{GB}/D_L = 10^{-4}$, 10^{-3}, and 10^{-2}.

terms of the competition to decrease the overall system free energy between the two processes occurring at the GB junction with the liquid solder: (a) IMC formation controlled by the GB diffusion and (b) reduction of the GB area in order to meet the force balance. The latter is accompanied by the dissolution of the IMC into the liquid solder, which requires the bulk diffusion in the liquid solder, thereby enhancing the penetration of the liquid solder, whereas the former reduces the liquid solder penetration. Therefore, as the D_{GB}/D_L ratio decreases, the latter process becomes more dominant and, consequently, the liquid solder penetrates deeper into the IMC GB. However, even if $\sigma_{GB} > 2\sigma_{L/\eta}$, the liquid solder does not penetrate completely up to the Cu pad, since the rate of the former process is inversely proportional to Z_{GB}.

As shown in Fig. 2, the thickness ratio, Z_{GB}/Z_c, does not change significantly during the growth of the IMC. Since the IMC formation rate at the GB junction decreases with increasing Z_{GB}, this implies that the IMC dissolution rate is also lowered as the penetration depth ($Z_c - Z_{GB}$) of the liquid solder increases. This is attributed to the curvature effect of the liquid solder/IMC interface. The curvature of the L/η interface has the opposite sign at the center of the IMC grain and the GB junction. As the penetration depth increases, the difference in curvature between the two positions increases and, thus, the composition gradient along the liquid solder channel between the IMC grains is reduced, so that the IMC dissolution rate at the GB junction decreases.

Effect of the solder/IMC interface energy ($\sigma_{L/\eta}$)

Even in the case where the diffusivity ratio, D_{GB}/D_L, is sufficiently small, the penetration of the liquid solder in between the IMC grains can be limited by the force balance at the GB junction with the liquid solder. This is because there is no driving force for the liquid solder to penetrate further into the IMC GB if the force balance governed by the Young–Laplace equation is satisfied at the GB junction. Therefore, the simulations were carried out for three different cases, viz. $2\sigma_{L/\eta} < \sigma_{GB}$, $2\sigma_{L/\eta} = \sigma_{GB}$, and $2\sigma_{L/\eta} > \sigma_{GB}$, by varying L/η interface energy ($\sigma_{L/\eta}$). Except for the value of $\sigma_{L/\eta}$, the three cases are identical, with the material parameters given in Table I (i.e., $\overline{D}_{GB} = 10^{-4}$ and $\sigma_{GB} = 300$ mJ/m^2) being used.

Figure 3 shows the η-IMC microstructures at $\tau = 5 \times 10^3$ and 5×10^4 and for the three different cases: $\sigma_{L/\eta} = 100$ mJ/m^2, 150 mJ/m^2, and 250 mJ/m^2. The corresponding changes in the thickness ratio, Z_{GB}/Z_c, with time for these three cases are shown in Fig. 4. The scallop-type IMC morphology with deep penetration of the liquid solder between the IMC grains is obtained only for the case where $\sigma_{L/\eta} = 100$ mJ/m^2, for which the complete wetting condition, $2\sigma_{L/\eta} < \sigma_{GB}$, is satisfied. With increasing $\sigma_{L/\eta}$, the liquid solder penetration becomes shallower and the IMC morphology comes to have an increasingly layer-type morphology.

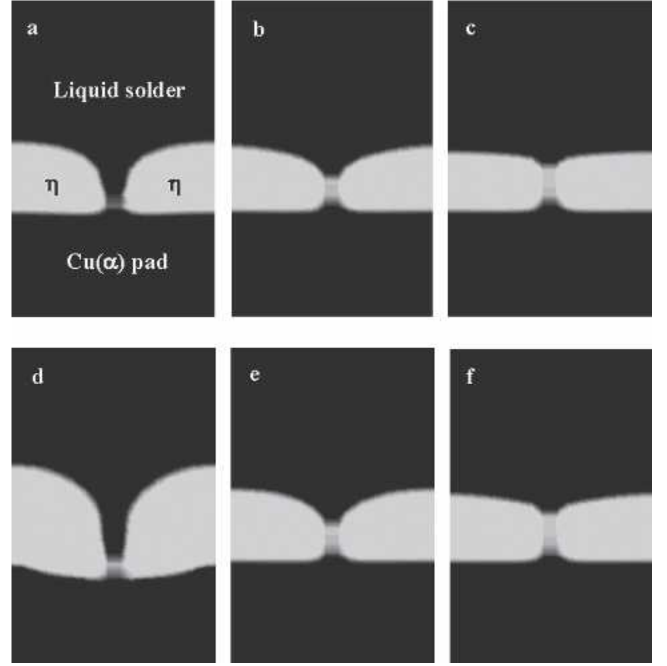

Fig. 3. Morphological evolutions of the η-IMC at 250°C for the three different cases of the liquid solder/IMC interface energy: (a) and (d) $\sigma_{L/\eta} = 100$ mJ/m^2, (b) and (e) $\sigma_{L/\eta} = 150$ mJ/m^2, and (c) and (f) $\sigma_{L/\eta} = 250$ mJ/m^2. Two snapshots for each of the three cases are shown as obtained at the nondimensional times: (a)–(c) $\tau = 5 \times 10^3$ and (d)–(f) $\tau = 5 \times 10^4$. $D_{GB}/D_L = 10^{-4}$ and $\sigma_{GB} = 300$ mJ/m^2 are assumed for all three cases.

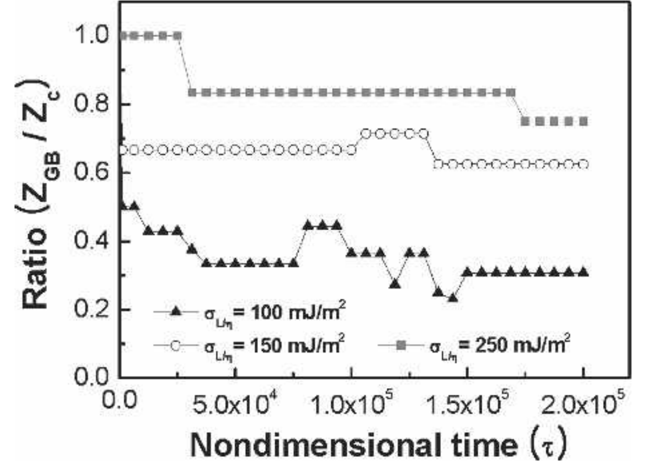

Fig. 4. Changes in the ratio of the IMC thickness along the GB (Z_{GB}) to that at the center of a grain (Z_c) with nondimensional time for the three cases: $\sigma_{L/\eta} = 100$ mJ/m^2, 150 mJ/m^2, and 250 mJ/m^2.

It is emphasized that the complete wetting condition of $2\sigma_{L/\eta} < \sigma_{GB}$ is a necessary, but not sufficient, condition for the formation of a scallop-type IMC morphology. In addition, as shown in Fig. 1, the diffusivity ratio, D_{GB}/D_L, must be sufficiently small for scallop-type IMC to be formed. Both of these conditions should be satisfied in most soldering processes to form the η-IMC. However, since $\sigma_{L/\eta}$ and D_L are changed to $\sigma_{S/\eta}$ and D_S, respectively, in the subsequent solid-state aging process, at least one of these conditions may not be satisfied, so that the scallop-type η-IMC morphology changes to a layer-type one.

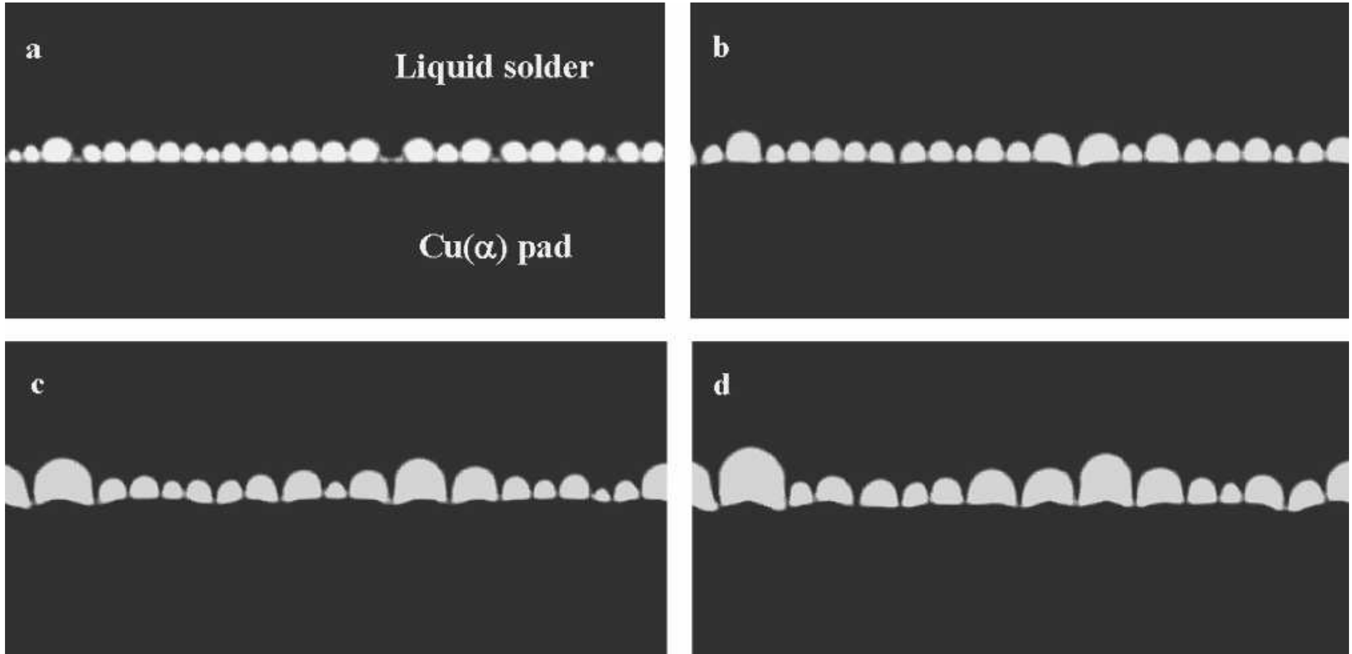

Fig. 5. The microstructural evolution of the η-IMC at 250°C for the case where $\sigma_{L/\eta}$ = 100 mJ/m^2 is depicted for the nondimensional times: (a) $\tau = 5 \times 10^3$, (b) $\tau = 1 \times 10^4$, (c) $\tau = 3 \times 10^4$, and (d) $\tau = 5 \times 10^4$. The IMC has a scallop-type morphology with a deep solder penetration between the IMC grains, and the scallop-type IMC grains coarsen but decrease in number concurrently with the IMC growth.

Figure 3 also shows that the IMC grows more rapidly in the case where $\sigma_{L/\eta}$ = 100 mJ/m^2. This is the consequence of the deep liquid solder penetration, which results in a reduction in the distance (Z_{GB}) required for the GB diffusion that is the rate-limiting step for IMC growth. The interplay between the IMC growth kinetics and the IMC morphology is further discussed in the following subsections.

Influence of the Morphology on the IMC Growth Kinetics during Soldering

Since the η-IMC layer formed between the liquid solder and Cu pad grows with concurrent coarsening among the IMC grains, the simulations to examine the IMC growth kinetics were carried out using a computational cell (184h × 90h) initially containing the 30 random-sized IMC grains (N = 30). In order to examine the influence of the IMC morphology on the growth kinetics, we here compare the IMC growth kinetics at 250°C between the two cases where $\sigma_{L/\eta}$ = 100 mJ/m^2 and 250 mJ/m^2 and, while keeping $\underline{D}_{GB} = 10^{-4}$ and σ_{GB} = 300 mJ/m^2 constant.

Figures 5 and 6 show a series of snapshots of the growth evolution of the η-IMC grains for the cases where $\sigma_{L/\eta}$ = 100 mJ/m^2 and 250 mJ/m^2, respectively, at different times: $\tau = 5 \times 10^3$, 1×10^4, 3×10^4, and 5×10^4 in Fig. 5; and $\tau = 5 \times 10^3$ and 5×10^4 in Fig. 6. As shown previously in Fig. 3, the IMC morphology is of the scallop type in the case where $\sigma_{L/\eta}$ = 100 mJ/m^2, whereas it is closer to a layer-type morphology when $\sigma_{L/\eta}$ = 250 mJ/m^2. From a comparison of the microstructural evolutions in Figs. 5 and 6, it can be seen that both the IMC growth and the concurrent coarsening of the IMC grains are enhanced when there is a deep penetration of the liquid solder in between the IMC grains.

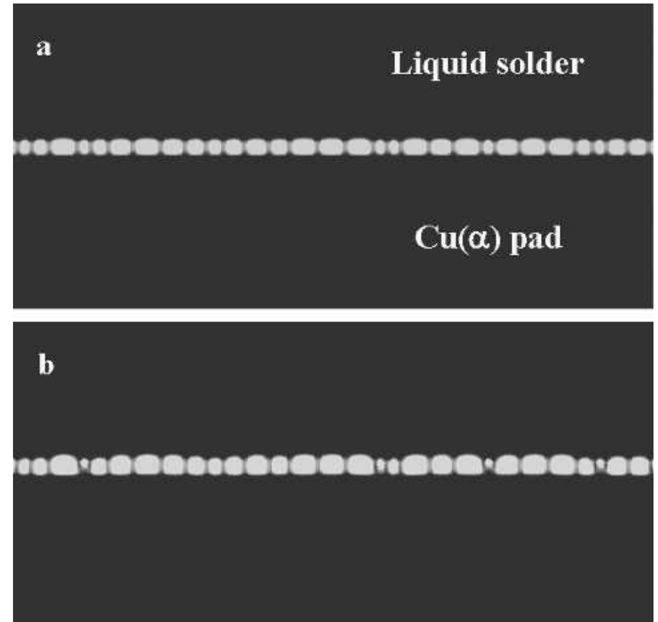

Fig. 6. The microstructural evolution of the η-IMC at 250°C for the case where $\sigma_{L/\eta}$ = 250 mJ/m^2 is depicted for the nondimensional times: (a) $\tau = 5 \times 10^3$ and (b) $\tau = 5 \times 10^4$. Other than the liquid solder/IMC interface energy, $\sigma_{L/\eta}$, the same material parameters as those for Fig. 5 are assumed for this system. The IMC morphology is more like a layer-type morphology without any deep solder penetration between the IMC grains, which results in a lowered IMC growth rate and negligible coarsening of the IMC grains.

It is noted that the enhanced IMC growth is a consequence, rather than the cause, of the scallop-type IMC morphology. The faster coarsening rate in the case of the lower $\sigma_{L/\eta}$ value is due to the increased L/η interface curvature caused by the solder penetration.

Figure 7 compares the changes in the (nondimensional) IMC thickness ($\bar{Z}$) with time for the two cases, $\sigma_{L/\eta} = 100$ mJ/m^2 and $\sigma_{L/\eta} = 250$ mJ/m^2. The IMC thickness was obtained by dividing the total area of the IMC grains by the lateral size (184*h*) of the system. The slight decrease in the IMC thickness in the initial stage for the case where $\sigma_{L/\eta} = 100$ mJ/m^2 is due to the dissolution of the IMC caused by the curvature effect, as the initially flat solder/IMC interface becomes rounded by the liquid solder penetration into the IMC GB. As measured in the "normal" stage following the initial transient stage, the temporal growth exponent of the IMC thickness, n, for $\bar{Z} \propto \tau^n$ is much lower in the case where $\sigma_{L/\eta} = 100$ mJ/m^2, owing to the concurrent coarsening of the IMC grains.[9,13,16] It is interesting to note that, although the IMC growth rate is enhanced by the formation of the scallop-type IMC morphology, the average IMC growth rate ($\Delta\bar{Z}/\Delta\tau$) is only increased by about a factor of 2, not by an order of magnitude. Since the limited increase in the average IMC growth rate is correlated to the difference in the value of Z_{GB} between the two cases, this is a clear indication that the rate-limiting step for IMC growth in the soldering reaction is the mass flux through the IMC GB diffusion.

If $\sigma_{L/\eta}$ is lowered still further below 100 mJ/m^2, the IMC growth rate will increase even more, as the deeper penetration of the liquid solder between the IMC scallops shortens the GB diffusion distance (Z_{GB}). However, below a certain critical value of $\sigma_{L/\eta}$, the concurrent coarsening of the IMC scallops will become retarded, because the change in the L/η interface curvature is not large enough to overcome the decrease in $\sigma_{L/\eta}$ and, thus, the temporal growth exponent, n, will increase toward n = 0.5.

IMC Growth Kinetics in Soldering Reaction and Solid-State Aging Process

In order to examine the changes in the IMC morphology and the IMC growth kinetics during the subsequent solid-state aging process a short time after the soldering reaction, simulations were carried out under soldering conditions at 250°C until the simulation time reached $\tau = 5 \times 10^4$ and then under solid-state aging conditions at 180°C for $\tau = 5 \times 10^4$. The material parameters employed for the soldering reaction and the subsequent solid-state aging process are those given in Table I. That is, at the simulation time of $\tau = 5 \times 10^4$, the solder diffusivity is decreased by four orders of magnitude from $\bar{D}_L = 1$ to $\bar{D}_S = 10^{-4}$, the IMC GB diffusivity is decreased by one order of magnitude, and the solder/IMC interface energy is increased from 100 mJ/m^2 to 250 mJ/m^2. Considering the Cu in the supersaturated solder precipitates as η-IMC particles within the bulk solder upon solidification, the composition in the solder region of $\phi_{N+1} = 1$ is also changed to the equilibrium solder composition at 180°C, c_S^{Sn}, at the start of the subsequent solid-state aging process ($\tau = 5 \times 10^4$). It is noted that, as calculated from the chemical free energy functions employed in the current study, the standard Gibbs free energies of η-IMC formation at 250°C and 180°C have approximately the same value of 7.1 kJ/mole.

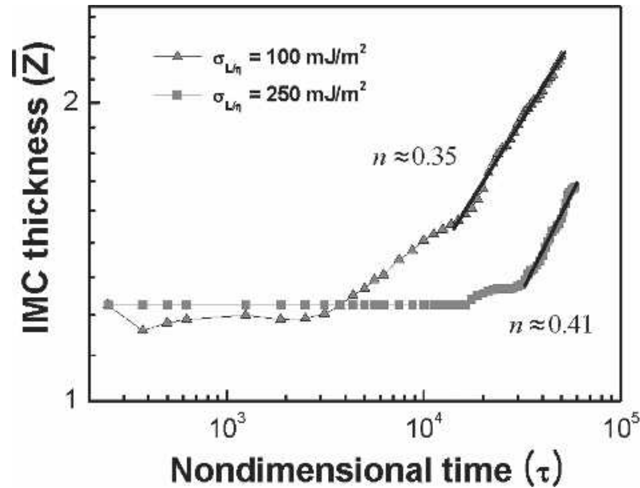

Fig. 7. Changes in the average IMC thickness ($\bar{Z}$) with nondimensional time for the cases where $\sigma_{L/\eta} = 100$ mJ/m^2 and 250 mJ/m^2, corresponding to Figs. 5 and 6, respectively. The temporal growth exponents, n, were determined in the normal stages of IMC growth.

Figure 8 shows a series of snapshots of the microstructural evolution of the η-IMC at different times, $\tau = 5 \times 10^3$ and 5×10^4, under soldering conditions, and $\tau = 1 \times 10^6$, 5×10^6, and 2.5×10^7, under solid-state aging conditions. As shown previously in Fig. 5, the IMC grows with scallop-type morphology under the soldering conditions and the IMC scallops coarsen concurrently. When the scallop-type η-IMC enters the solid-state aging conditions at $\tau = 5 \times 10^4$, as shown in Fig. 8c, the first change to occur is the morphological evolution from a scallop type to a layer type, due to the Cu flux from the top of the IMC scallops to the valley between the IMC scallops. Then, the layer-type IMC grows with a much reduced rate and there is negligible coarsening among the IMC grains. The formation of the layer-type IMC morphology is plausible in the subsequent solid-state aging process since, in addition to the partial wetting condition of $2\sigma_{S/\eta} > \sigma_{GB}$, the diffusivity ratio between the IMC GB and the solid solder is as large as $D_{GB}/D_S = 10^{-1}$.

Figure 9 shows the change in the IMC thickness ($\bar{Z}$) with time. Because of the negligible concurrent coarsening of the IMC grains, the temporal growth exponent (n) in the solid-state aging process approaches 0.5, which is typical of diffusion-limited growth. The average growth rate of the IMC thickness, $\Delta\bar{Z}/\Delta\tau$, was found to be $\sim 2 \times 10^{-5}$ in the soldering reaction and $\sim 10^{-7}$ in the subsequent solid-state aging process. Thus, there is an approximately two orders of magnitude difference in the IMC growth rate between the solder reaction and the subsequent aging process.

The lowered IMC growth rate in the subsequent solid-state aging process is predominantly due to the morphological change of the IMC to the layer type

Fig. 8. The microstructural evolution of the η-IMC during the soldering reaction at 250°C for $\tau \leq 5 \times 10^4$ and during the subsequent solid-state aging process at 180°C for $\tau > 5 \times 10^4$ is depicted for the nondimensional times: (a) $\tau = 5 \times 10^3$ and (b) $\tau = 5 \times 10^4$ under the soldering conditions; and (c) $\tau = 1 \times 10^6$, (d) $\tau = 5 \times 10^6$, and (e) $\tau = 2.5 \times 10^7$ under the aging conditions. The IMC changes from a scallop-type to a layer-type morphology during the subsequent aging process after the soldering reaction.

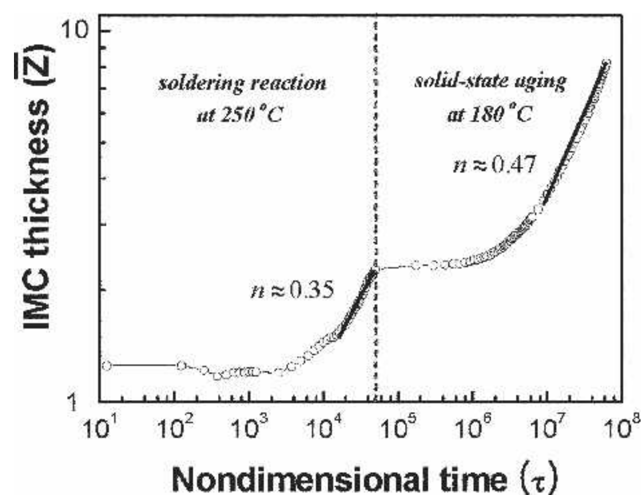

Fig. 9. Change in the average IMC thickness ($\overline{Z}$) with nondimensional time during the soldering reaction ($\tau \leq 5 \times 10^4$) and during the subsequent solid-state aging process ($\tau > 5 \times 10^4$).

and the lowered GB diffusivity. The rate-limiting step for IMC growth in both the soldering and aging conditions is the mass flux through the IMC GB diffusion, and the GB diffusion distance (Z_{GB}) increases almost linearly with the IMC thickness ($\overline{Z}$): $Z_{GB} \approx 0.3\overline{Z}$ in the soldering reaction and $Z_{GB} \approx \overline{Z}$ in the solid-state aging process. Therefore, one can obtain the relation for the IMC growth rate, $d\overline{Z}/d\tau \propto \overline{D}_{GB}/Z_{GB}$, on the bases of $\overline{Z} \approx \sqrt{\overline{D}_{GB}\tau}$ and $Z_{GB} \propto \overline{Z}$. Owing to the morphological change of the IMC scallops to the layer type in the early stages of the subsequent aging process, the average value of Z_{GB} in the solid-state aging process for $\tau = 5 \times 10^7$ is approximately one order of magnitude larger than that in the soldering reaction for $\tau = 5 \times 10^4$. This difference in Z_{GB}, together with the difference in $\overline{D}_{GB}$, results in an IMC growth rate in the subsequent solid-state aging process that is slower by two orders of magnitude.

It is noted that, although the solder diffusivity in the subsequent solid-state aging process was reduced by four orders of magnitude, the solder diffusivity itself has only a minor influence on the growth rate of the layer-type IMC in the solid-state aging process. Even when the solid solder diffusivity at $\tau = 5 \times 10^4$ was changed to $\overline{D}_S = 10^{-3}$ or $\overline{D}_S = 10^{-5}$,

nearly the same result was obtained as that for $\overline{D}_S = 10^{-4}$ shown in Fig. 9.

CONCLUSIONS

Using a multiphase field model, the morphological and growth evolutions of the η-IMC formed between a Sn-based solder and a Cu pad have been studied for the soldering reaction and the subsequent solid-state aging process. The morphology of the growing η-IMC is governed by a competition between the IMC formation rate controlled by GB diffusion and the IMC dissolution rate controlled by solder penetration, which reduces the high energy GB area. Therefore, the complete wetting condition between the solder/IMC interface energy and the IMC GB energy is a necessary, but not sufficient, condition for the formation of the scallop-type IMC morphology with deep solder penetration between the IMC grains. In addition, for the formation of the scallop-type IMC, it is required that the solder diffusivity be greater than the GB diffusivity of the IMC.

The morphological change of the IMC from a scallop type to a layer type during the subsequent solid-state aging process after the soldering reaction results in drastic changes in the IMC growth kinetics. First, the temporal growth exponent of the IMC thickness approaches 0.5, owing to the negligible concurrent coarsening of the IMC grains. Second, the growth rate decreases by several orders of magnitude, primarily due to the increased length of the GB diffusion, which is the rate-limiting step for IMC growth. However, the solder diffusivity, which is reduced by several orders of magnitude in the subsequent solid-state aging process, has only a minor influence on the growth kinetics of the layer-type IMC.

ACKNOWLEDGEMENT

We are grateful to Professor K.N. Tu for motivating us to perform this work.

REFERENCES

1. D.R. Frear and P.T. Vianco, *Metall. Mater. Trans. A* 25A, 1059 (1994).
2. C.Y. Liu, C. Chen, A.K. Mai, and K.N. Tu, *J. Appl. Phys.* 85, 1 (1999).
3. C.H. Zhong and S. Yi, *Soldering Surf. Mount. Technol.* 11, 44 (1999).
4. K.S. Kim, S.H. Huh, and K. Suganuma, *J. Alloys Compounds* 352, 226 (2003).
5. S.K. Kang, R.S. Rai, and S. Purushothaman, *J. Electron. Mater.* 25, 1113 (1996).
6. W.K. Choi and H.M. Lee, *J. Electron. Mater.* 29, 1207 (2000).
7. K.N. Tu and K. Zeng, *Mater. Sci. Eng. R* 34, 1 (2001).
8. T.Y. Lee, W.J. Choi, K.N. Tu, J.W. Jang, S.M. Kuo, J.K. Lin, D.R. Frear, K. Zeng, and J.K. Kivilahti, *J. Mater. Res.* 17, 291 (2002).
9. H.K. Kim and K.N. Tu, *Phys. Rev. B: Condens. Matter Mater. Phys.* 53, 16027 (1996).
10. K.N. Tu, T.Y. Lee, J.W. Jang, L. Li, D.R. Frear, K. Zeng, and J.K. Kivilahti, *J. Appl. Phys.* 85, 4843 (2001).
11. K.N. Tu, F. Ku, and T.Y. Lee, *J. Electron. Mater.* 30, 1129 (2001).
12. H.K. Kim, H.K. Liou, and K.N. Tu, *Appl. Phys. Lett.* 66, 2337 (1995).
13. M. Schaefer, R.A. Fournelle, and J. Liang, *J. Electron. Mater.* 27, 1167 (1998).
14. W. Yang, R.W. Messler, Jr., and L.E. Felton, *J. Electron. Mater.* 23, 765 (1994).
15. S. Choi, J.P. Lucas, K.N. Subramanian, and T.R. Bieler, *J. Mater. Sci.: Mater. Electron.* 11, 497 (2000).
16. J.Y. Huh, K.K. Hong, Y.B. Kim, and K.T. Kim, *J. Electron. Mater.* 33, 1161 (2004).
17. I. Steinbach and F. Pezzolla, *Physica D* 134, 385 (1999).
18. S.G. Kim, W.T. Kim, T. Suzuki, and M. Ode, *J. Cryst. Growth* 261, 135 (2004).
19. J.H. Shim, C.S. Oh, B.J. Lee, and D.N. Lee, *Z. Metallkd.* 87, 205 (1996).